SIA

XPS imaging Investigations of pitting corrosion mechanisms in Inconel 600

B. A. Kobe,[1]* S. Ramamurthy,[1] M. C. Biesinger,[1] N. S. McIntyre[1] and A. M. Brennenstühl[2]

[1] Surface Science Western, Room G-1, Western Science Centre, University of Western Ontario, London, Ontario N6A 5B7, Canada
[2] Ontario Power Generation Inc., 700 University Avenue, Toronto, Ontario M5W 1E6, Canada

The surface chemistry associated with pitting corrosion on a nickel-based alloy, Inconel 600, has been studied using imaging x-ray photoelectron spectroscopy. The irregularity of the sample surfaces necessitated a more elaborate background correction than is usually applied in such imaging. Areas of active pitting were found to contain corrosion products that are high in chromium oxide and depleted in nickel and iron. Sites of anodic activity on the surface were able to be defined more clearly using principal component analysis. Elements that are dissolved preferentially are deposited cathodically within well-defined regions whose distance from the anodic pit appears related to the open-circuit potential. Copyright © 2005 John Wiley & Sons, Ltd.

INTRODUCTION

This paper has two themes: a study of corrosion mechanisms that assist the pitting of Inconel 600 under hydrothermal conditions; and the assessment of XPS and Auger electron spectroscopy (AES) imaging methods to characterize such processes. X-ray photoelectron spectroscopy imaging has been of increasing interest to the surface analysis community with the emergence of commercial spectrometers equipped with the capability for resolving the origin of photoelectrons spatially separated on a surface by a few microns. Chemical specificity is the distinct advantage of photoelectron spectroscopy imaging over the equivalent AES and secondary ion mass spectroscopy (SIMS) techniques, but the low photoelectron emittance could lead to unacceptably low image contrast, particularly if a narrow bandpass is required to resolve closely placed chemical states. Also, the high backgrounds associated with some XPS spectra could lead to false contrast from areas with different extrinsic loss contributions. These latter challenges are particularly severe on rough nickel alloy surfaces affected by pitting corrosion; chemical shifts of interest are <2 eV and the extrinsic loss structure for the most intense metal 2p lines is high. Thus, part of this work has sought background correction remedies that could be applied to such images. Also, the most effective use of chemical shift information has been sought, in light of the need to acquire such images over times considerably longer than those used for other surface techniques. Finally, advantages of XPS imaging other than chemical effects are explored for these particular surfaces.

Localized corrosion is initiated and sustained by electrochemical couples that drive an anodic dissolution of metal and a cathodic deposition of corrosion products at sites adjacent to the anode. The chemical potential driving the reaction is created by local differences in impurity or defect concentration. Thus, microscopic surface analysis is quite important to any diagnosis of the causes of the corrosion failure. The present case concerns pitting attack during its use as a nuclear boiler heat-exchanger alloy in contact with pressurized water at 280 °C. Of primary interest is the mechanism that gave rise to the corrosion cell, the size of the cell and evolution of the cell as the pitting reaction progressed. X-ray photoelectron spectroscopy imaging was used recently to study localized corrosion of a nickel–copper alloy, and microscopic anodic and cathodic electrodes were identified.[1] This present study will explore in greater detail the possible methodologies for improving the quality of XPS imaging information and will compare its content with that provided by AES. The primary cause of the pitting process is shown to be sulphate/sulphide attack of the surface leading to an anodic dissolution of the alloy within highly localized regions.

EXPERIMENTAL

Autoclave exposures

A drawing of the segmented probe arrangement used during this investigation to simulate tube/tube sheet crevice conditions that exist in a boiler is presented in Fig. 1.[2] The alloy 600 steam generator tube is at the centre of the probe and is surrounded by 15 carbon steel rings. A crevice of 1 mm between the inside surface of the tube and the rings was filled with reagent-grade magnetite powder. This arrangement has allowed corrosion monitoring to be carried out at five locations through the crevice depth of 54 mm. These locations

*Correspondence to: B. A. Kobe, Surface Science Western, Room G-1, Western Science Centre, University of Western Ontario, London, Ontario N6A 5B7, Canada. E-mail: bkobe@surf.ssw.uwo.ca
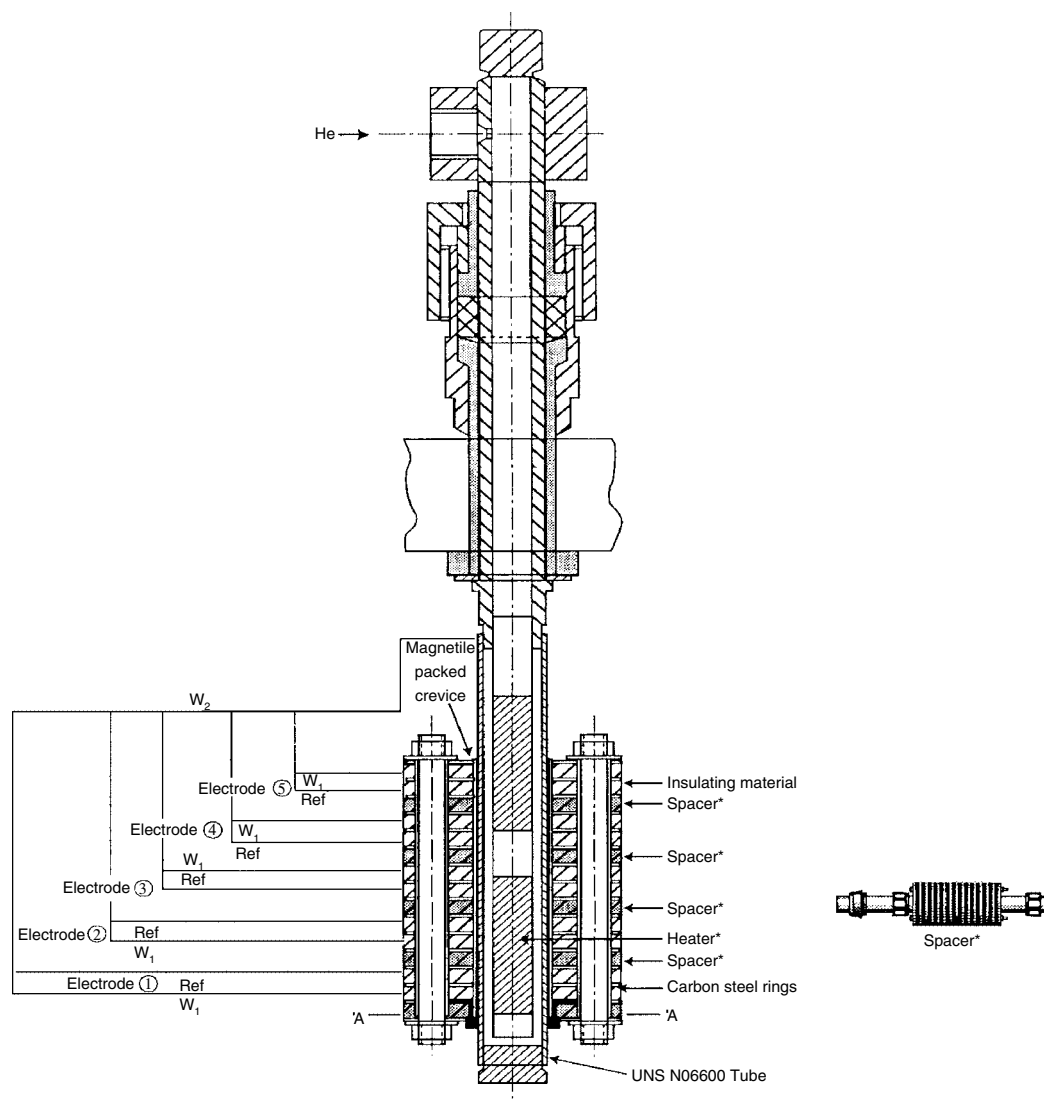
Figure 1. A section through the segmented probe used to simulate crevice conditions in a boiler.

Table 1. Matrix of conditions for Inconel 600 test probes

Sample	Crevice location	Chloride (ppb)	Oxygen (ppb)	Sulphate (ppm)	Salts	Hydrazine (ppb)	Time (h)	Temperature (°C)
A	E3	—	200	—	Yes	200	650	305
B	E3	100	200	10	Yes	200	450	295
C	E1	—	400	—	No	—	450	295
D	E1	—	200	—	Yes	200	650	305

have been identified as E1, E2, E3, E4 and E5, with location E5 at the mouth of the crevice and location E1 at the bottom of the crevice.

Several factors were investigated during this study: time, temperature, presence/absence of balanced salts, chloride, sulphate, dissolved oxygen, hydrazine concentration, number of on/off heat flux cycles and crevice location. Factor levels were selected that, for the most part, might be expected in service. The matrix selected to determine the effect of these factors is presented in Table 1.[2] However, it should be noted that the hideout process increases the impurity concentration by a factor of $10^5–10^6$.[3]

Electrochemical testing was carried out in a refreshed 4 l capacity UNS N06600 autoclave with a refreshment rate of 10 ml min^{-1}. The liquid volume in the autoclave at the laboratory ambient temperature was 3 l for all of the test environments. A conditioning phase was carried out prior to running the chemistries given in Table 1. This conditioning consisted of a 48 h exposure to demineralized water with 100 ppb of N_2H_4, adjusted to pH 9.5 with NH_4OH and with the dissolved oxygen adjusted to a level of <5 ppb. This chemistry was also run for 24 h at the end of the excursion.

After the autoclave exposures had been completed, the test probe was carefully removed and sectioned down the

axis of the tube, thus revealing the sludge-filled crevice and facilitating the removal of sludge. The two halves of the test probe were then sectioned circumferentially to give pieces of tube that corresponded to the five locations. Each piece was ~11 mm long. Loose deposits were removed from the surface of the tube by ultrasonic cleaning in isopropyl alcohol. The electrodes then were examined using a light microscope; a magnification of 50× was used at first to locate areas of corrosion damage. Areas exhibiting pits were then examined at higher magnifications to confirm that they were indeed the result of corrosion. This was followed by a detailed examination using the surface analytical techniques described below.

The XPS instrumentation

The XPS analyses were carried out with a Kratos Axis Ultra spectrometer using a monochromatic Al Kα source (15 mA, 14 kV). The instrument work function was calibrated to give a binding energy of 83.96 eV for the Au $4f_{7/2}$ line for metallic gold and the spectrometer dispersion was adjusted to give a binding energy of 932.6 eV for the Cu $2p_{3/2}$ line of metallic copper. The base pressure was 10^{-10} Torr and the operating pressure was 10^{-9} Torr. The Kratos charge neutralizer system was used on all specimens with a filament current of 1.6 A and a charge balance of 2.4 V. Elemental and chemical-state XPS images were collected using low magnification mode (~800 × 800 µm) and imaging aperture 2. The elemental maps were collected using a pass energy of 160 eV with collection times varying from 1800 to 3600 s, depending on the peak intensity. The oxygen chemical-state maps were collected using a pass energy of 40 eV and the nickel chemical-state maps were collected using pass energies of 40 and 20 eV. An XPS spot analysis of selected areas was carried out with a spot of ~220 µm. High-resolution spectra of all major species were taken using a 40 eV pass energy with a step of 0.1 eV. Prior to XPS analysis the samples were cleaned ultrasonically in acetone and then in methanol.

Background correction

The XPS images were corrected for inelastic background and surface topography using Boolean operations in the VISION2 processing software from Kratos. To correct the XPS images it was necessary to collect a background image ~10 eV below the main peak for each image. The images were first corrected for the inelastic background by subtracting the background image from the main image (S − B). Finally, the subtracted image, (S − B)/B, was divided by the background to remove any effects due to topography.

Principal component analysis

Principal component analysis (PCA) was carried out using PLS_Toolbox 2.1 from Eignevector Research running on Matlab 6.0. The XPS images were converted to VAMAS file format using the VISION2 processing software (Kratos). The image data then were converted to ASCII data using a custom-written Matlab routine (courtesy of K. Artyushkova, Kent State University; modified by B.A. Kobe and M.C. Biesinger), resulting in a 256 × 256 data set for each image. Each separate image is then added to a larger matrix

($256 \times 256 \times n$, where n is the number of images), which is used by image PCA software in PLS_Toolbox. Principal component analysis was carried out using the 'auto' scaling option. This feature first mean-centres the data and then each mean-centred variable is divided by its standard deviation, which results in variables with unit variance. Further examples and information on image PCA can be found elsewhere.[4−9]

Auger electron spectroscopy

The AES analyses were performed using a 10 keV electron beam rastered over a 500 × 500 µm area. A 5 s sputter was required to remove the outer surface contamination. This was expected to have removed a layer ~1.5 nm thick. Auger imaging was performed by monitoring the intensities of the peak and the background energies for various elements of interest. Surface topography effects were minimized using the following routine: (peak − background)/(background)$^{1/2}$.

RESULTS

The XPS spectra and images were obtained for samples that had been exposed to hydrothermal conditions as described above. The presence or absence of several possible coolant contaminants (see Table 1) on local surface corrosion was explored as a function of location on the sample with respect to a carbon steel ring that simulated the tube sheet region of a boiler. Locations close to the bottom of a crevice are expected to be influenced by higher galvanic currents and therefore more intense local electrode activity. Accordingly, these results are organized into studies of locations on samples: (a) near the bottom of the crevice (E1); (b) the middle of the crevice (E3). Auger and XPS spectra had been recorded previously for macroscopic areas of these samples; the compositions obtained show that the general surface composition is nickel-rich.[2] This would indicate that the average surface site is responding to a basic coolant chemistry. A SEM investigation of these samples revealed localized pitting to depths of several micrometres; such pitting would be considered serious in heat-exchanger tubing. The present imaging studies have concentrated on the localized analysis of these pits and the regions immediately surrounding them, to reveal the effects of local rather than generalized chemistry.

E3 positions

Figure 2(a) is a SEM image of a cluster of pit defects in sample A (see Table 1 for treatment conditions). The defect consists of several deep pits surrounded by a number of shallower depressions. The remaining parts of this figure show the effects of different background processing algorithms on the Ni 2p signal intensity. Comparison of the raw XPS images of the pit area for Ni 2p (Fig. 2(b)) and the corresponding background (Fig. 2(c)) show a gradation of the pixel intensity across the images. In general, the lower right portions of the two images have a higher pixel intensity compared to the upper left areas of the images. The Ni 2p image does not show clearly the distribution of the nickel due to the
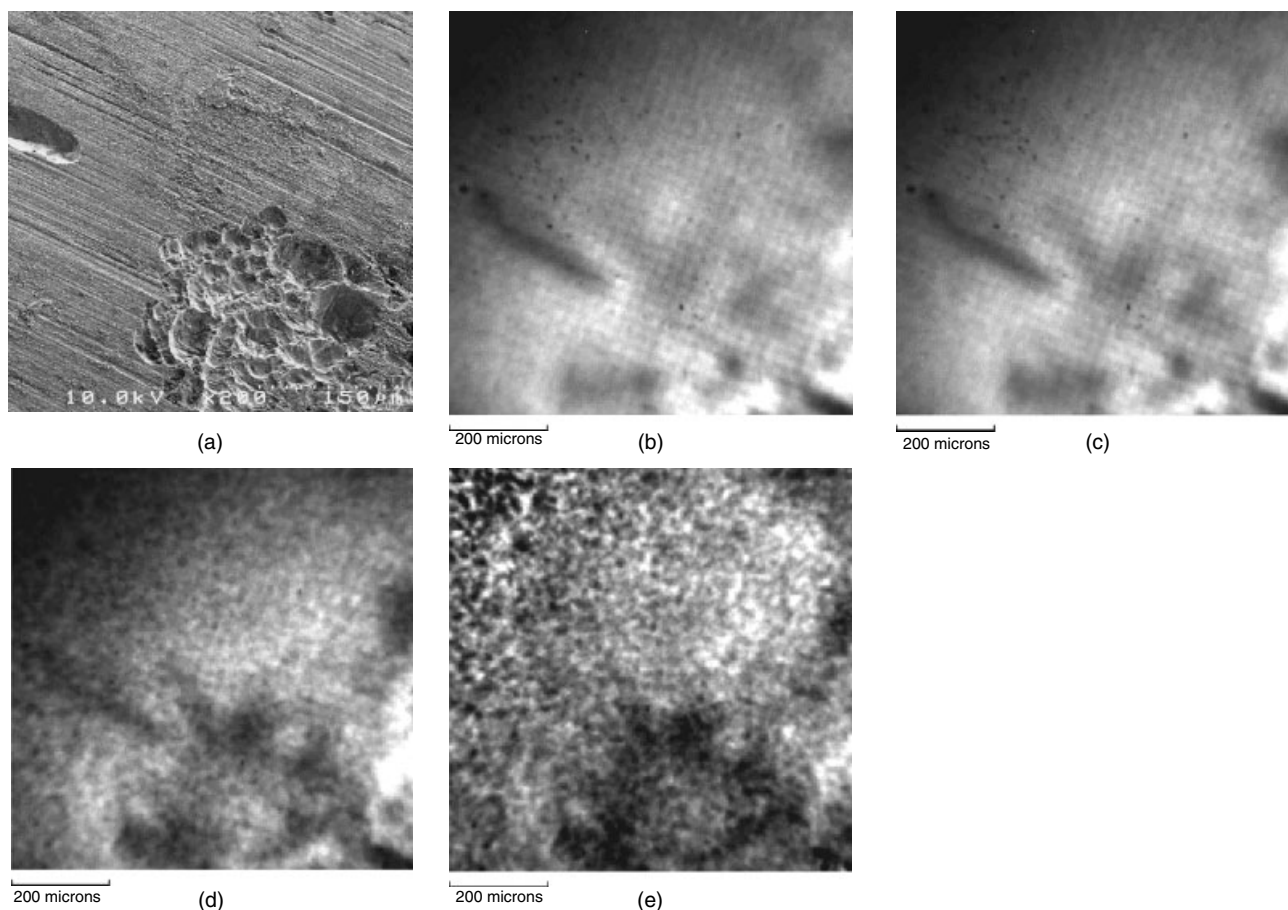
Figure 2. The XPS image processing technique used to remove the effects of background at the Ni $2p_{3/2}$ peak in sample A: (a) SEM image of the pit region studied by XPS imaging; (b) original Ni $2p_{3/2}$ XPS image; (c) background image taken $\sim$10 V below the Ni $2p_{3/2}$ peak maximum; (d) Ni $2p_{3/2}$ S − B correction using the instrument software; (e) Ni $2p_{3/2}$ (S − B)/B correction.

inelastic background and topographic effects. To remove the inelastic background, the background image was subtracted from the Ni 2p image (S − B) and the resulting image is presented in Fig. 2(d).[10] The subtracted image more clearly defines the pit region and the distribution of nickel outside the pit. However, the contrast across the image is still present due to the curvature of the samples. Division of the image by the background has been used to correct SIMS[11] and Auger[12] images for surface roughness, and a similar routine has been applied here to these XPS images. The use of (S − B)/B results in an image (Fig. 2(e)) that has little detectable topographic contrast and, with elemental contrast dominant, an element-specific image is produced. Such a correction process results in a severely depressed signal with the attendant need to acquire images for much longer counting times in order to attain an adequate signal-to-noise ratio.

The XPS spectra for the Ni 2p, Cr 2p, O1s, C 1s and S 2p lines were taken using a 220 µm sampling area both inside the pit area (Fig. 3(a)) and for an area well away from the pit (Fig. 3(b)). Inside the pit, at least two different chemical forms of nickel are detected: metallic nickel at 852.9 eV and a nickel Ni(OH)$_2$ species at $\sim$855.8 eV. The metal phase is detected because the hydroxide overlayer is very thin. The Ni 2p spectrum for the region outside the pit (Fig. 3(b)) shows only one species; the binding energy (855.9 eV) as well as the

separation and shape of the shake-up peak suggests that this is also Ni(OH)$_2$.[13,14] The O 1s spectrum for both areas shows two species present in differing quantities: substitutional oxide oxygen (530.4 eV) and surface hydroxide (532.0 eV). The Cr 2p spectrum in the pitted region is assigned to Cr$_2$O$_3$ on the basis of its binding energy and peak shape.[15] The S 2p spectra showed that both sulphate and sulphide species were present in low concentrations in both areas of sample A. Further detailed analysis of the sulphur chemistry was done using spectra with a higher signal-to-noise ratio. In the fitted spectra shown in Fig. 4, four different chemical species are identified from their S $2p_{3/2}$ binding energies: monosulphide, polysulphide, sulphite and sulphate. All of these species are identified in varying concentrations, both within the pit and in a region well away from the pit. Because the originating source for the sulphur is almost certainly sulphates dissolved in the aqueous phase during the reaction, the appearance of sulphides suggests that microscopic sites with strong reducing potentials exist throughout the regions surveyed. Reaction sites for sulphur must have smaller dimensions than the scales measured for anodic dissolution and cathodic deposition, because the same range of sulphur species exists through both the anodic and cathodic regions. Variation on a small scale is possible when it is realized that the localized potential will migrate constantly during the reaction, leaving a number of reduction products.
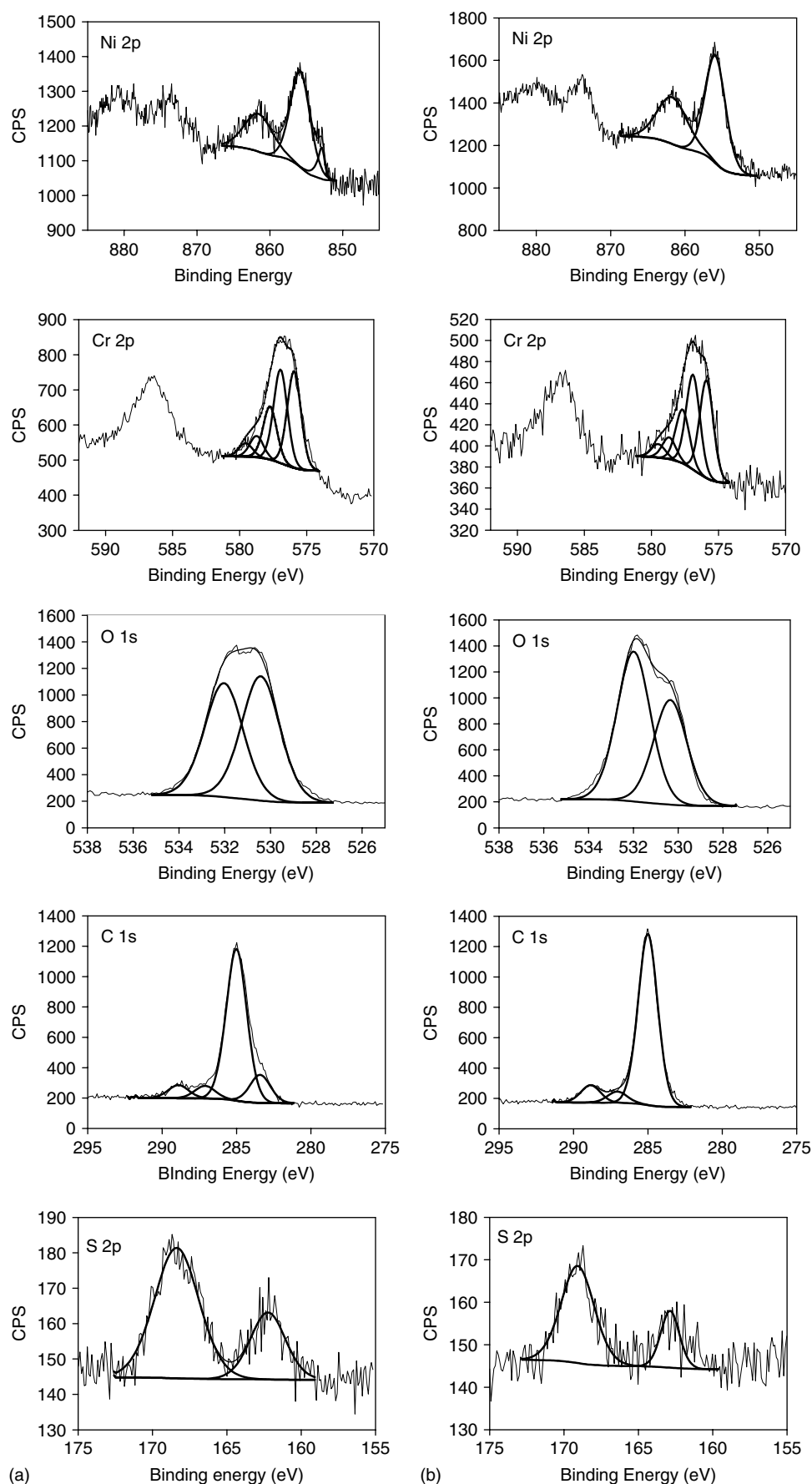
Figure 3. The XPS spectra taken with a 220 µm aperture of Ni 2p, Cr 2p, O 1s, C 1s and S 2p lines for sample A: (a) inside the pit region shown in Fig. 2; (b) outside the pit region (in the upper centre of Fig. 2). All spectral positions have been corrected for charging to a C 1s binding energy of 285.0 eV.
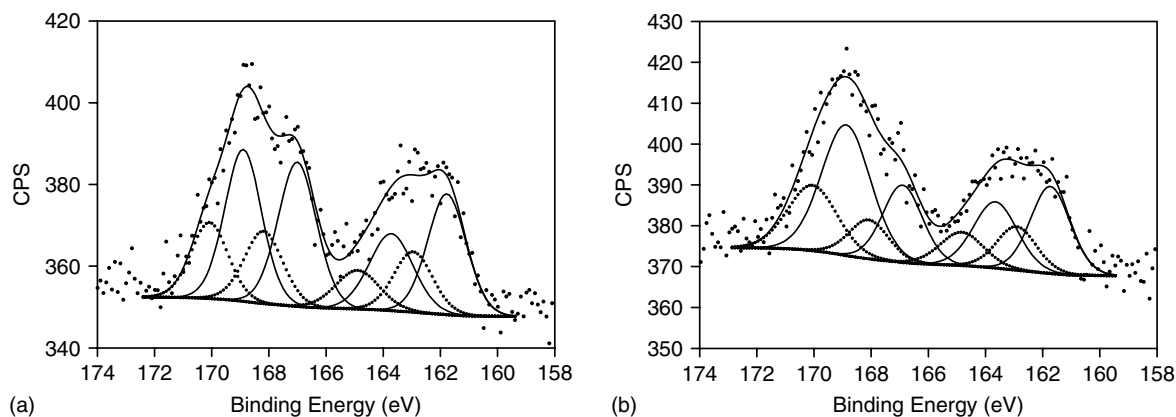
Figure 4. The XPS spectra taken with a 220 μm aperture for the S 2p lines for sample A: (a) inside the pit region; (b) outside the pit region. Only the S $2p_{3/2}$ fitted components are shown.

The elemental and chemical species were mapped for sample A using appropriate portions of the Cr $2p_{3/2}$, Fe $2p_{3/2}$, S $2p_{3/2}$, Ni $2p_{3/2}$, Ni (hydroxide), Ni (metal), O 1s, O (oxide) and O (hydroxide) spectra (Figs 5(b)–5(j)). The 'grey scale' of photoelectron intensities represents a range of 1–256 (black through to white). The scale for each image is adjusted to give maximum contrast, thus a black-appearing region does not necessarily indicate that no intensity is contributed from that element but rather that it is considerably lower than elsewhere in the image. Figure 5(a), the SEM image of the region, is again shown but in this case features are marked to show their relationships to the elemental and chemical maps. Within the general pit region, the inner portion (region i) has the highest chromium intensity (Fig. 5(b)), whereas iron (Fig. 5(c)) and nickel (Fig. 5(e)) are generally located around the pit. Within region i, intensities for iron (Fig. 5(c)) and nickel hydroxide (Fig. 5(g)) are lower than elsewhere in the image; however the image for nickel metal (Fig. 5(f)) intensity is coincident with much of the chromium intensity distribution. We interpret these distributions as the result of anodic oxidation and subsequent dissolution of nickel and iron, leaving a thin chromium oxide surface layer overlying the base nickel alloy. The very thin chromium oxide film is deduced from the fact that the underlying nickel metal phase is detectable. Region ii comprises the border of the chromium-intense region within which sulphur (Fig. 5(d)) is most intense; sulphur, present as both sulphide and sulphate, could act as a corrosion initiator, leading to a gradually expanded circle of pits. In contrast to sulphur and chromium, the intensity for iron is most intense in a large region at the left-hand side of the image (region iii). The nickel hydroxide intensity is highest in another discrete region in the upper right portion of the image (region iv). We interpret these latter intensities to be the result of back-precipitation of nickel and iron species at cathodic sites neighbouring the anodic pit. The precipitation of nickel and iron species would be governed by the presence of a cathodic potential equal to or greater than the half-cell potential for their particular reactions. For this sample condition and area the depositions occur in diffuse, but not entirely identical, regions that surround the pit. However, other electrochemical couples may be active, as outlined below.

An alternative analysis of the same XPS raw (unprocessed) images was carried out on the five major elements using a PCA routine. The chemical-state maps from samples A and D were not included in the PCA because they were taken using a different pass energy compared with the elemental maps. The objective was to discover common correlations or anti-correlations among different elements from the principal components derived from an analysis of the photoelectron intensity variations throughout each image. Figures 6(a)–6(d) show the highest four principal components found in an analysis of the images for Ni $2p_{3/2}$, Fe $2p_{3/2}$, Cr $2p_{3/2}$, O 1s and S $2p_{3/2}$. The image score and corresponding factor loadings for the first principal component (Fig. 6(a)) identify regions with the most variation (93.2%). The factor loadings for all five elements are strongly correlated positive. This common correlation is attributed to several factors, including topographic effects due to the roughness and slight curvature of the tube samples, the inelastic photoelectron background and a grid pattern from the CCD detector. The second principal component (PC 2) shows regions where chromium and nickel are strongly anti-correlated, with the remaining elements not showing any significant correlation. The variation of PC 2 is only 3.9%, indicating that most of the variation is due to the topographic and background effects. Having removed these effects, the image score for PC 2 clearly identifies the chromium-rich region within the pit, which was also observed in the background-corrected XPS image (Fig. 5(b)). The strong presence of chromium and the absence of nickel suggests that this is a region of active anodic activity, where nickel dissolution and chromium retention are in progress. A small correlation between nickel and iron is also shown in PC 2, suggesting that iron is also undergoing dissolution.

The last two principal components (PC 3 and PC 4) represent a much smaller variation in the data but they do show subtle correlations between the elements not easily identified in the background-corrected XPS images. The percentage variations for PC 3 and PC 4 are 1.9% and 0.9%, respectively. The factor loadings for PC 3 show that nickel, iron and chromium are anti-correlated with oxygen and sulphur. The corresponding image score shows sulphur and oxygen located outside the pit region to the right of region
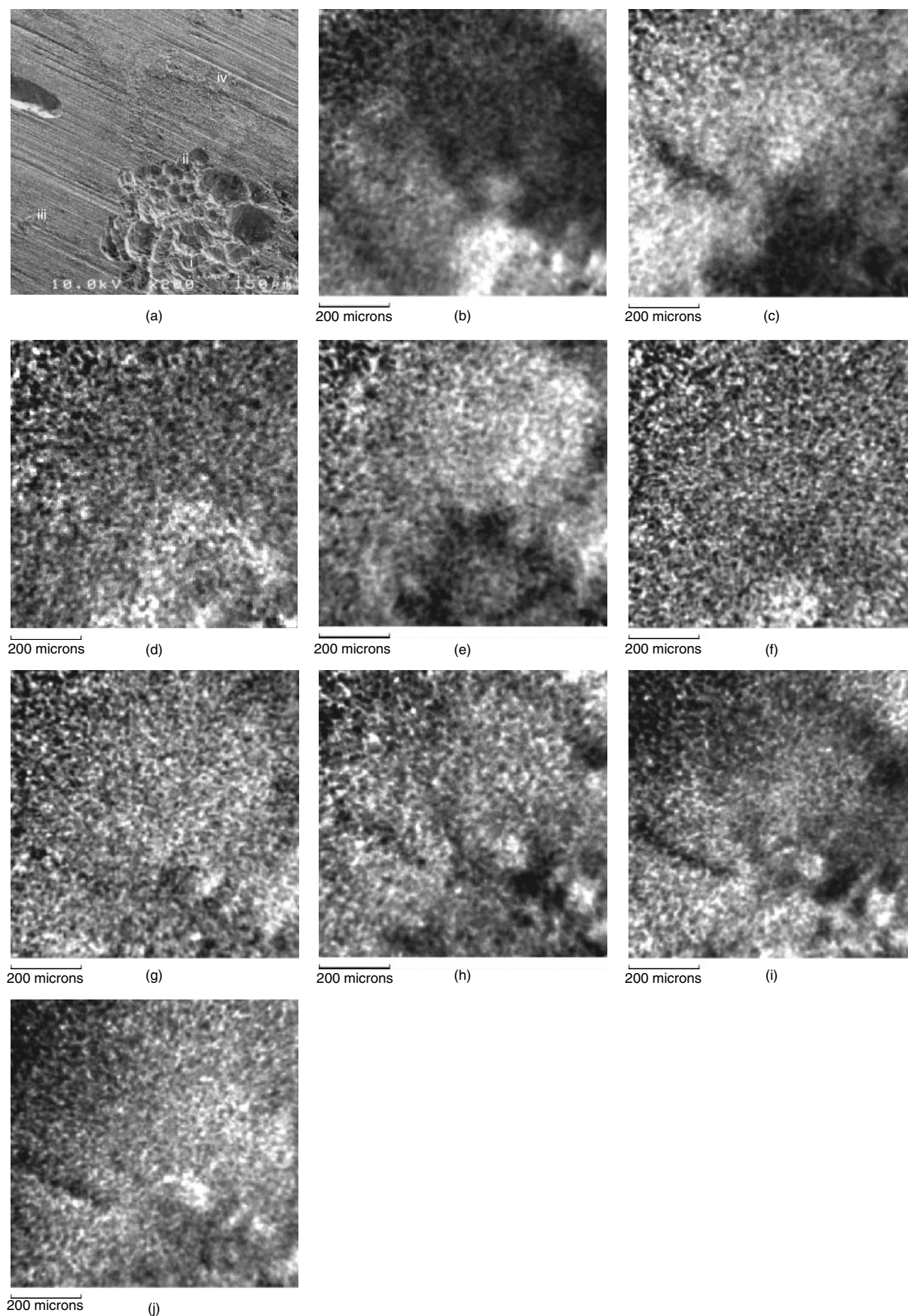
Figure 5. The SEM image and XPS elemental and chemical state images of a corrosion pit in sample A: (a) SEM image of pit region; (b) Cr $2p_{3/2}$ image; (c) Fe $2p_{3/2}$ image; (d) S $2p_{3/2}$ image; (e) Ni $2p_{3/2}$ image; (f) Ni $2p_{3/2}$ (metal) image; (g) Ni $2p_{3/2}$ (hydroxide) image; (h) O 1s image; (i) O 1s (oxide) image; (j) O 1s (hydroxide) image. Note, all images here and subsequently have been treated with the background division routine $(S - B)/B$.
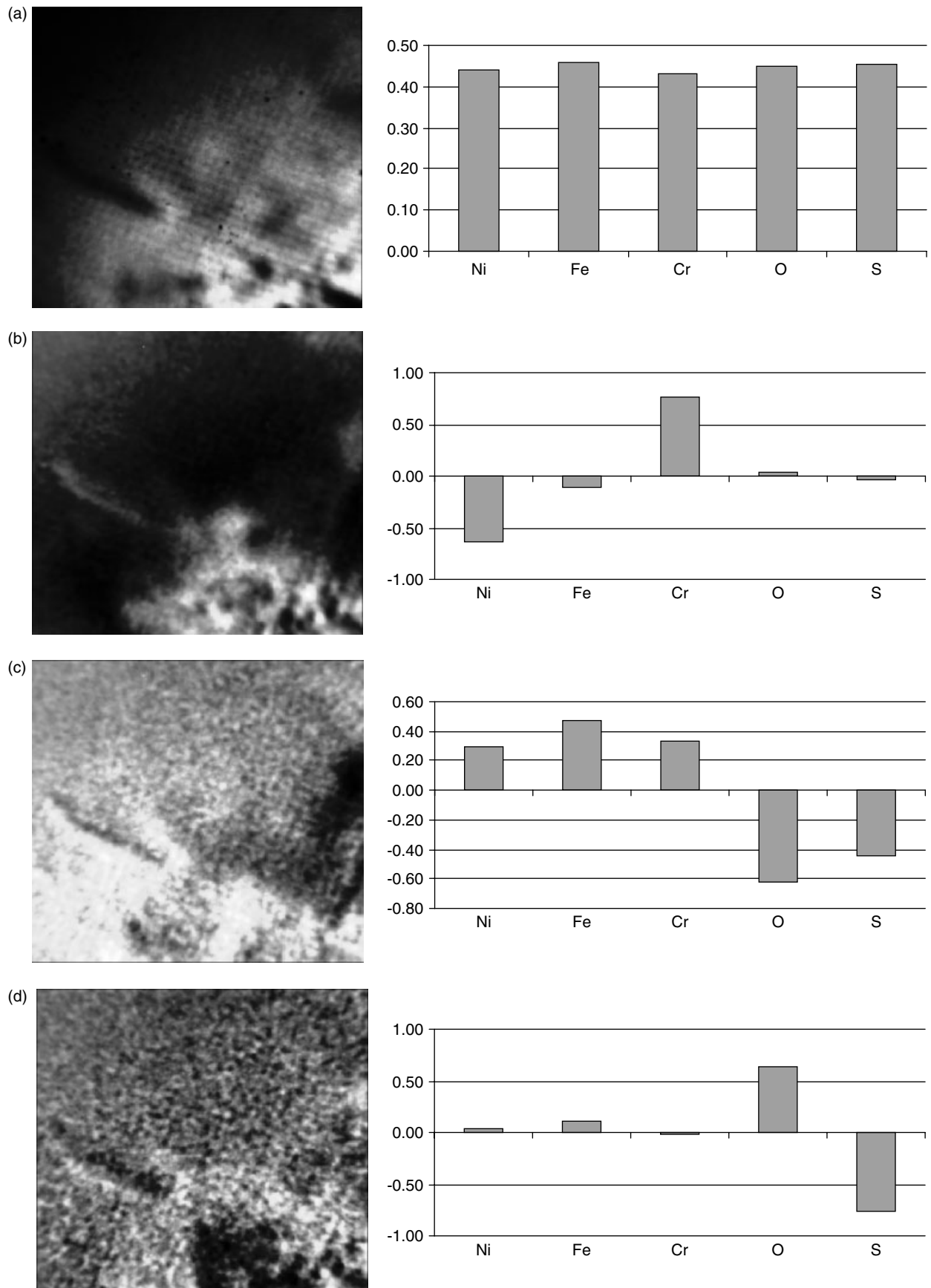
Figure 6. Principal component analysis of selected raw XPS images shown in Fig. 5. The four highest principal components are shown: (a) PC 1; (b) PC 2; (c) PC 3; (d) PC 4.

iv (Fig. 5(a)) and to a lesser extent around the edge of the pit. This suggests that the edge of the pit and the surrounding area may have more oxidized sulphur species present. For PC 4 there is a strong anti-correlation between oxygen and sulphur only; thus PC 4 represents the smallest amount of variation remaining. The oxygen is distributed around the edge of the pit and sulphur is located within the pit. This suggests that another sulphur species is present, possibly a reduced species such as a sulphide. It should be noted that the oxygen and sulphur seen in PC 4 represent the remaining oxygen and sulphur not represented in PC 3.

This same area was also studied using AES. No images of the corrosion product elements were able to be detected without using a 5 s ion bombardment to remove a masking layer of surface carbon. An approximation of the carbon layer removed would be 0.5–2 nm, depending upon the roughness of the region. The secondary electron image and Auger maps Cr LMM, Fe LMM, Ni LMM, O KLL and S KLL are presented in Figs 7(a)–7(f). The spatial resolution of the maps shown in Fig. 7 is clearly far superior to the images produced by XPS and enables us to distinguish clearly the distribution of various elements within the pitted region. For example, close examination of the nickel and chromium Auger maps indicates that chromium appears to be present at

the outer edges of the pits, whereas nickel is seen at the inner regions of the pit. Thus, the distribution of these elements appears to complement each other within the pitted region. Moreover, oxygen and sulphur maps indicate that these elements are associated with the regions where chromium has been observed. These results suggest that perhaps nickel is being depleted from the active regions and redepositing on adjacent sites, which could correspond to the locations where the balancing cathodic reactions could occur. The presence of sulphur and oxygen at the active (corroding) sites also indicates that these elements play an important role in the pitting corrosion behaviour of this material. Thus, the elemental distribution maps from the scanning Auger microprobe are very useful in distinguishing the distribution of elemental species within and outside the pitted region. However, the chemical nature of these species cannot be determined from the maps shown in Fig. 7.

An E3 site on another sample (sample B), shown in Fig. 8(a), was analysed by imaging XPS. Elemental maps for Cr $2p_{3/2}$, Fe $2p_{3/2}$, S $2p_{3/2}$, Ni $2p_{3/2}$ and O 1s are presented in Figs 8(b)–8(f). The Cr $2p_{3/2}$ image (Fig. 8(b)) shows its concentration within the pitted areas seen in Fig. 8(a), and sulphur is also seen to be concentrated within these areas (Fig. 8(d)). Iron is shown in Fig. 8(c) and presumed to be
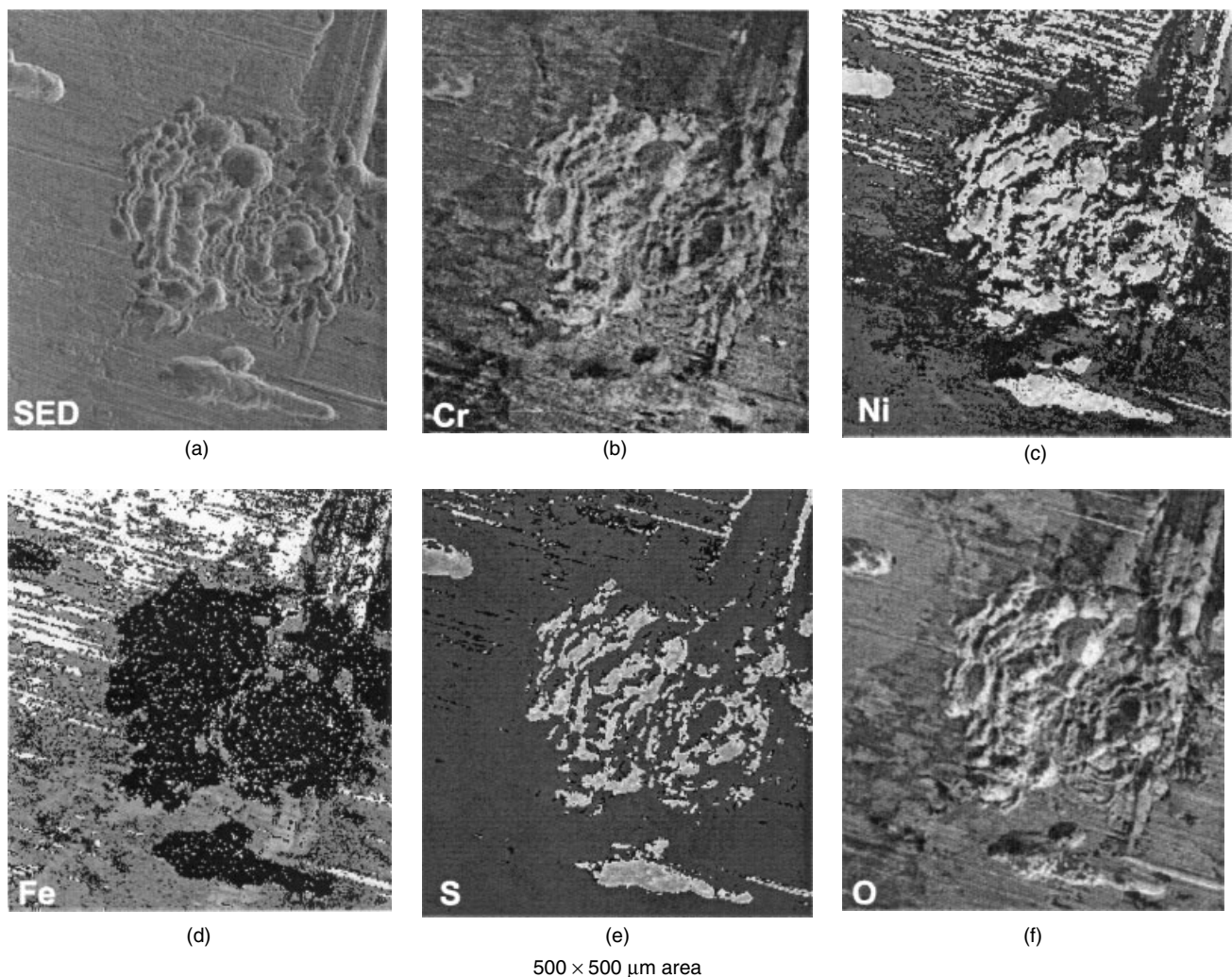

500 × 500 µm area

Figure 7. Auger maps of the pit in sample A: (a) Cr LMM; (b) Fe LMM; (c) Ni LMM; (d) O KLL; (e) S KLL.
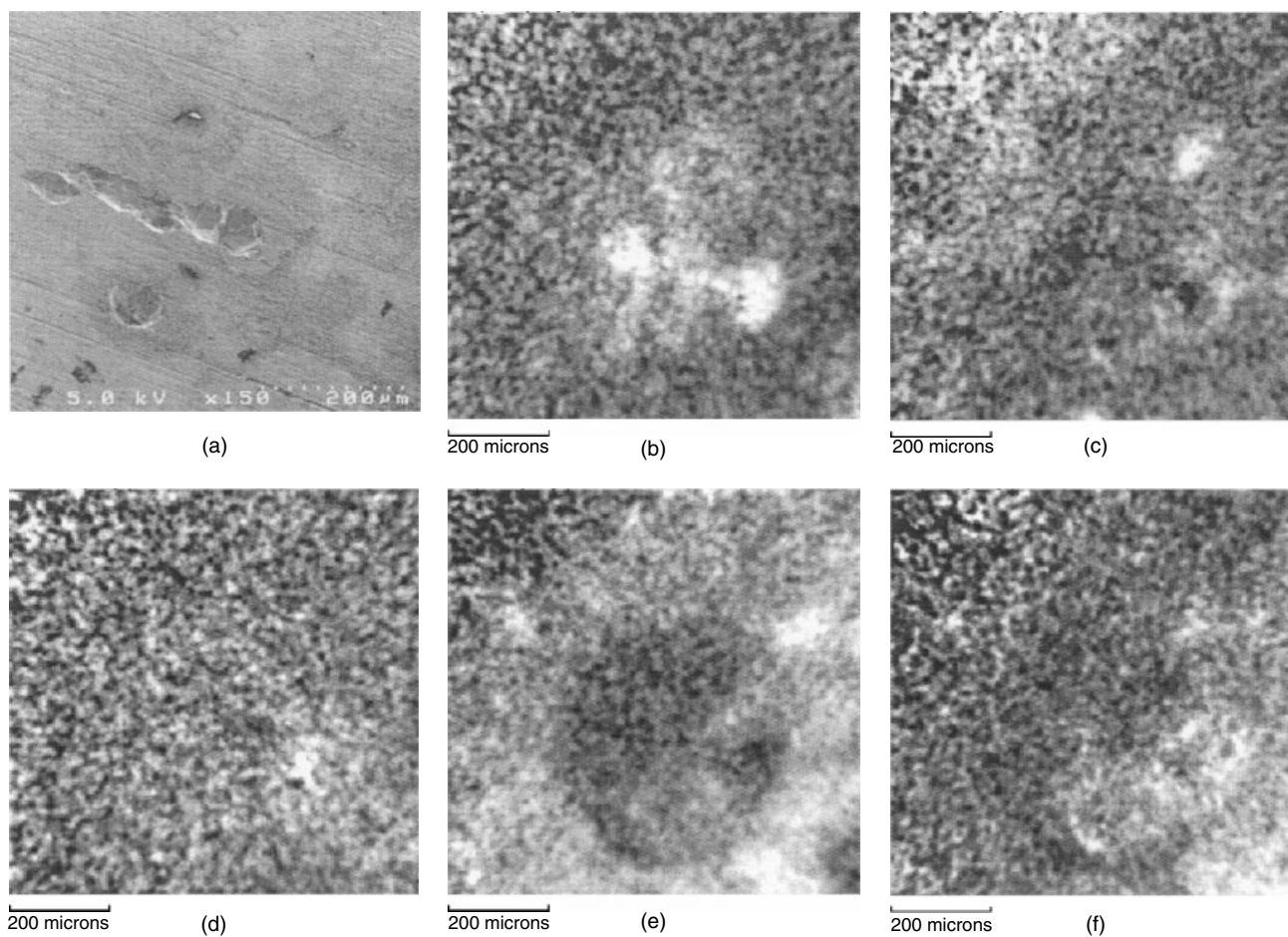
Figure 8. The SEM and XPS elemental images of a pit from sample B: (a) SEM image of the entire defect and the surrounding areas; (b) Cr $2p_{3/2}$ image; (c) Fe $2p_{3/2}$ image; (d) S $2p_{3/2}$ image; (e) Ni $2p_{3/2}$ image; (f) O 1s image.

precipitates from species dissolved in the anodic pits. Some of the deposits are very close to the anodic areas (along the rim of the pits), whereas others are in diffuse patches some hundreds of microns away. By contrast, the locus where nickel deposition (Fig. 8(e)) begins is well defined as a circle ~500 µm in diameter surrounding the anodic pit. Beyond this circle, deposition occurs fairly evenly over a broad area.

Principal component analysis of this same area is shown in Figs 9(a)–9(d). The four highest principal components are presented for Ni $2p_{3/2}$, Fe $2p_{3/2}$, Cr $2p_{3/2}$, O 1s and S $2p_{3/2}$. As seen previously, PC 1 represents the greatest variance (97.6%) present in the data and is responsible for removing the topographic effects, the photoelectron background and artifacts from the CCD detector. The variance of PC 2 (1.3%) is significantly lower than PC 1 and shows a strong anti-correlation between nickel and chromium, with chromium located in the pit. This trend is also present in the background-corrected images (Fig. 8). However, PC 2 also shows a slight correlation between oxygen and nickel. The remaining two principal components, PC 3 and PC 4, have variances of only 0.6 and 0.3%, respectively. Although they represent very small components of the variation in the data, they are included for comparison purposes. The factor loadings for PC 3 show a positive correlation for sulphur and a negative correlation for iron, nickel and chromium. These results would suggest that a reduced from the sulphur

is present. The image score shows that sulphur is generally located in the pit region and over the surface of the sample. For PC 4 there is an anti-correlation between oxygen and the other four elements.

E1 sites

A pitting defect in sample C (see Table 1) was also studied. The XPS elemental maps for Cr $2p_{3/2}$, Fe $2p_{3/2}$, S $2p_{3/2}$, Ni $2p_{3/2}$ and O 1s are shown in Figs 10(b)–10(f). As well as the greater distance from the counter-electrode, this sample had been exposed to a higher concentration of dissolved oxygen in the coolant. Figure 10(a) details two closely spaced pits and the surrounding region. The pit interiors are enriched in chromium (Fig. 10(b)), deficient in iron (Fig. 10(c)) and nickel (Fig. 10(e)) and there is a distribution of sulphur (Fig. 10(d)) around the edge of the pit. Of particular interest here are the patterns of precipitation of iron and nickel solution species; two concentric part-circles of iron and nickel closely surround the anodic pit region, closer than for pits in the E3 region, with most of the precipitated iron and nickel concentrated in such regions (Figs 10(d)–10(f)).

Figure 11 presents the four major principal components for Ni $2p_{3/2}$, Fe $2p_{3/2}$, Cr $2p_{3/2}$, O 1s and S $2p_{3/2}$. The first principal component represents the greatest variance of 87.5%. The factor loadings are all positive for each of the elements and represent effects from the topographic,
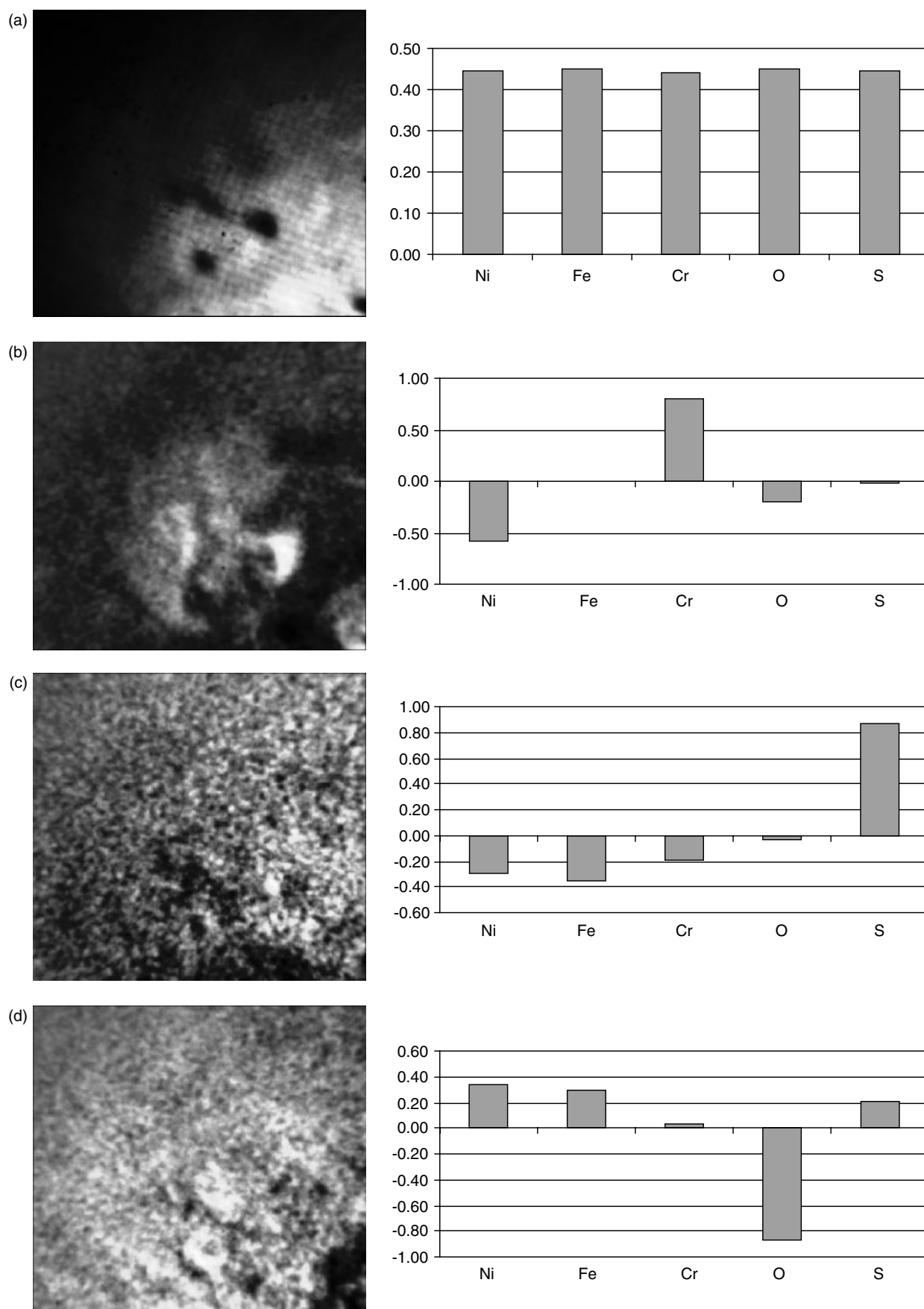
Figure 9. Principal component analysis of the raw images shown in Fig. 8. The four highest principal components are shown: (a) PC 1; (b) PC 2; (c) PC 3; (d) PC 4.
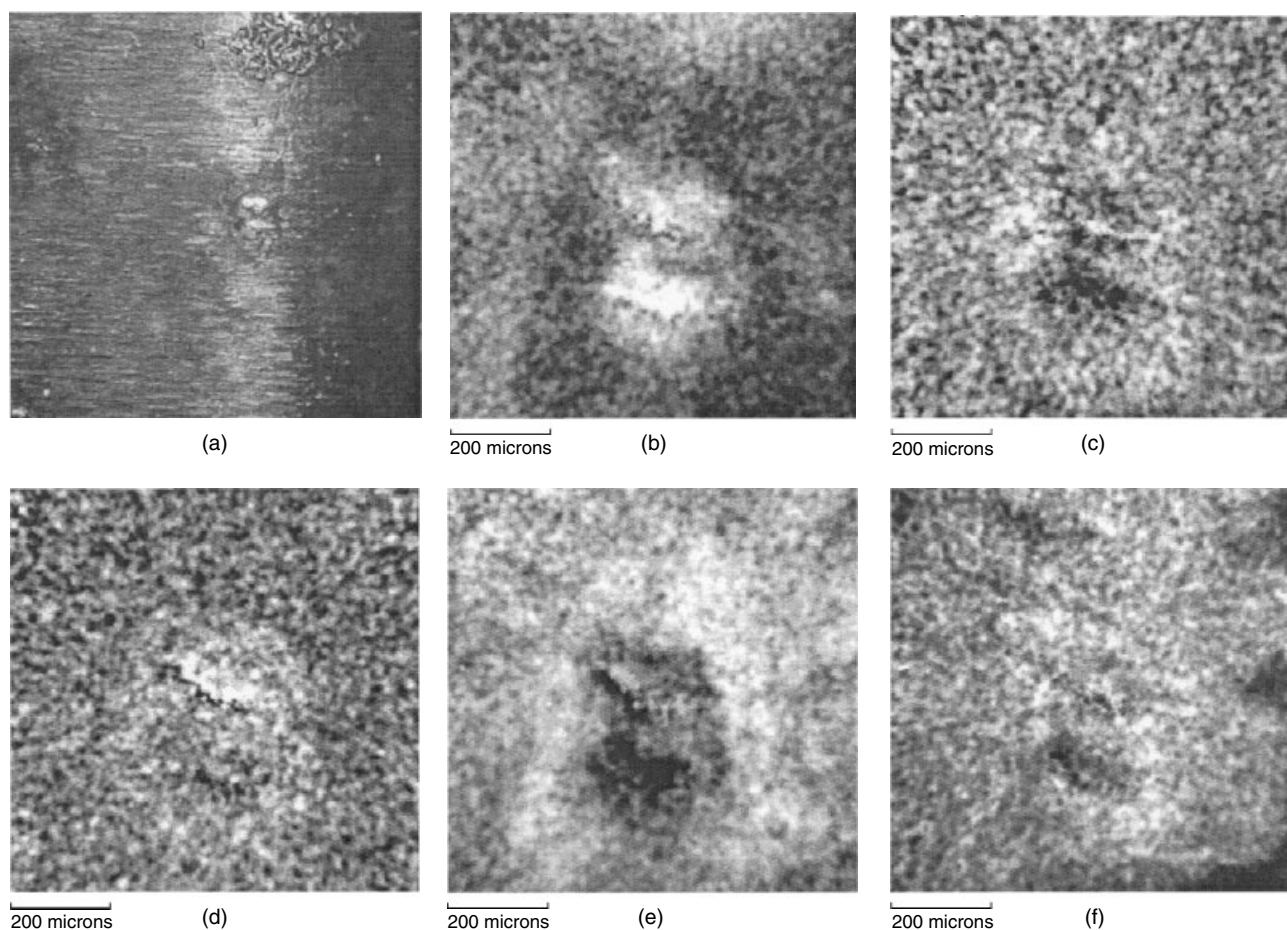
Figure 10. Optical microscope and elemental XPS images of a defect in sample C: (a) optical image of the defect and surrounding areas; (b) Cr $2p_{3/2}$ image; (c) Fe $2p_{3/2}$ image; (d) S $2p_{3/2}$ image; (e) Ni $2p_{3/2}$ image; (f) O 1s image.

photoelecton background and the CCD detector. The factor loadings for PC 2 (variance of 7.4%) show the greatest anti-correlation between nickel and chromium. The image score shows that chromium is located within the pit and nickel is deposited around the pit. This trend is also shown in the background-subtracted images (Fig. 10). With PC 3 the variance of 2.7% and the factor loadings show a strong anti-correlation between the sulphur and the other four elements, particularly nickel and iron. The image score shows a small area of sulphur (dark areas) located in the lower pit. However, the image score also suggests that the remaining four elements are concentrated in the pit region and to a lesser extent on the surface of the tube, suggesting the presence of metallic oxides and a reduced form of sulphur. The variance of 1.86% for PC 4 shows an anti-correlation between oxygen and mostly nickel and iron. The dark areas away from the pit represent areas of greater oxygen.

A dark, defective area of sample D in the shape of the numeral 1, with its base located in a mechanically produced groove or scratch (Fig. 12(a)), was also mapped. The XPS elemental and chemical images for Cr $2p_{3/2}$, Fe $2p_{3/2}$, S $2p_{3/2}$, Ni $2p_{3/2}$, Ni (hydroxide), Ni (metal), O 1s, O (oxide) and O (hydroxide) are shown in Figs 12(b)—12(j). The defect area is chromium-rich (Fig. 12(b)) and is again interpreted as an anodic site from which chromium and iron (Fig. 12(c)) have dissolved preferentially. These latter elements are found

to have deposited in different but well-delimited regions adjacent to the defect. In the case of nickel hydroxide (Fig. 12(g)), its deposition site is separate from the anodic sites. The image of metallic nickel (Fig. 12(f)) is strongest around the region of the scratch, suggesting that in this area a very thin coverage of chromium oxide exists. Note that XPS spot analyses (not shown) indicate the presence of chromium oxide within the defect area. The highest intensities for oxidic oxygen (Fig. 12(i)) are co-located with nickel hydroxide, whereas the oxhydroxide O 1s distribution (Fig. 12(j)) is most closely associated with the iron region, which is probably associated with a hydrolysed magnetite deposit.

The PCA results for the four major elements are presented in Fig. 13. The first principal component (variance of 93.8%) represents the combined effects of surface topography, photoelectron background and artifacts from the CCD detector. The second principal component (variance of 4.0%) shows that nickel and sulphur are anti-correlated with chromium and oxygen. These results are significantly different from those observed in the background-corrected images (Fig. 12). The background-corrected images show that the defect is chromium rich but the image score for PC 2 shows that most of the oxygen and chromium (bright areas) is located well to the right of the defect, with only a minor amount located within the defect area. These areas are most likely associated with a thin chromium oxide. The nickel
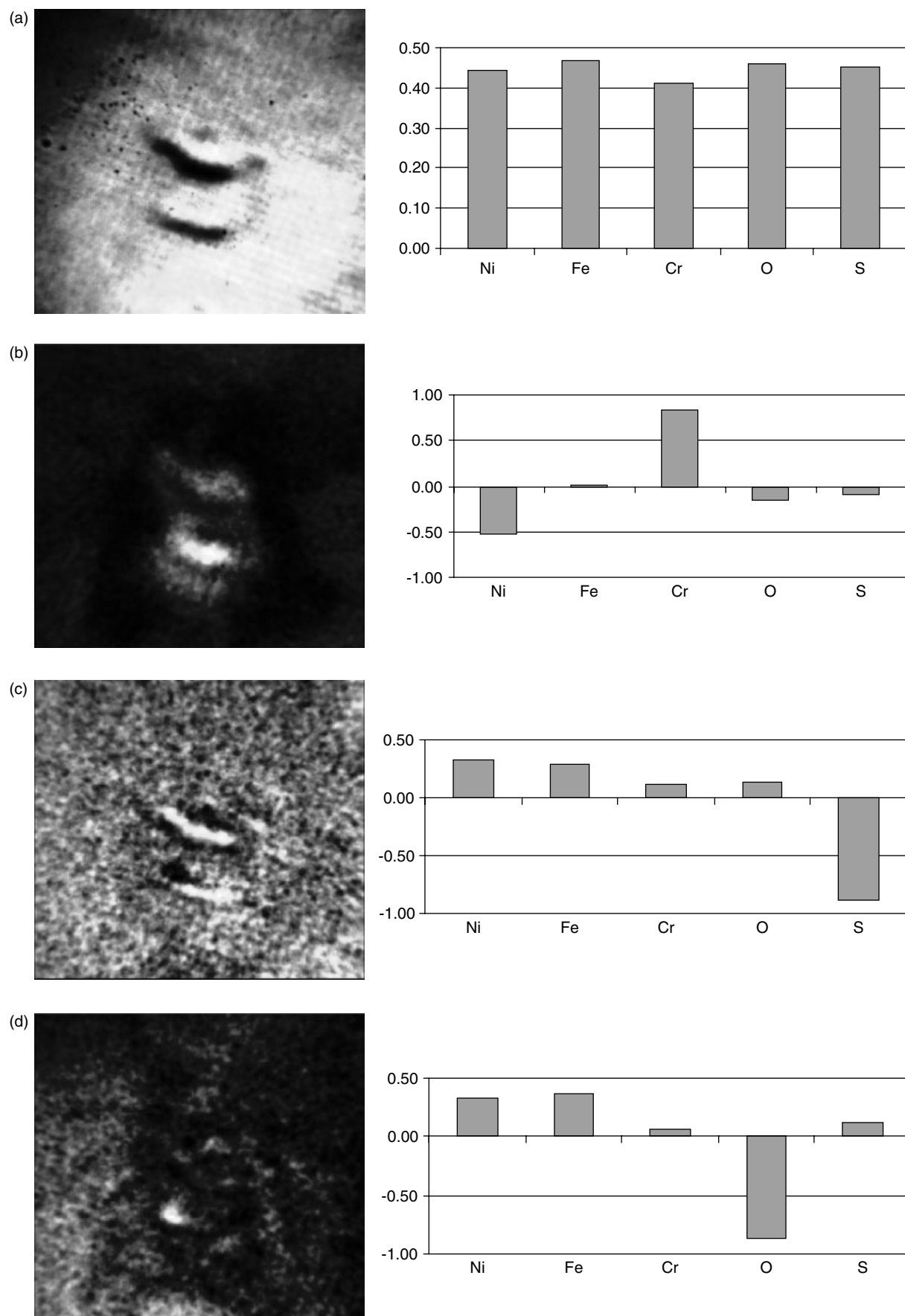
Figure 11. Principal component analysis of the raw images shown in Fig. 10. The four highest principal components are shown: (a) PC 1; (b) PC 2; (c) PC 3; (d) PC 4.

Figure 12. The SEM and XPS elemental and chemical state images of a defect in sample D: (a) SEM image of the defect and surrounding area; (b) Cr $2p_{3/2}$ image; (c) Fe $2p_{3/2}$ image; (d) S $2p_{3/2}$ image; (e) Ni $2p_{3/2}$ image; (f) Ni $2p_{3/2}$ (metal) image; (g) Ni $2p_{3/2}$ (hydroxide) image; (h) O 1s image; (i) O 1s (oxide) image; (j) O 1s (hydroxide) image.

Figure 13. Principal component analysis of the raw images shown in Fig. 12. The four highest principal components are shown: (a) PC 1; (b) PC 2; (c) PC 3; (d) PC 4.
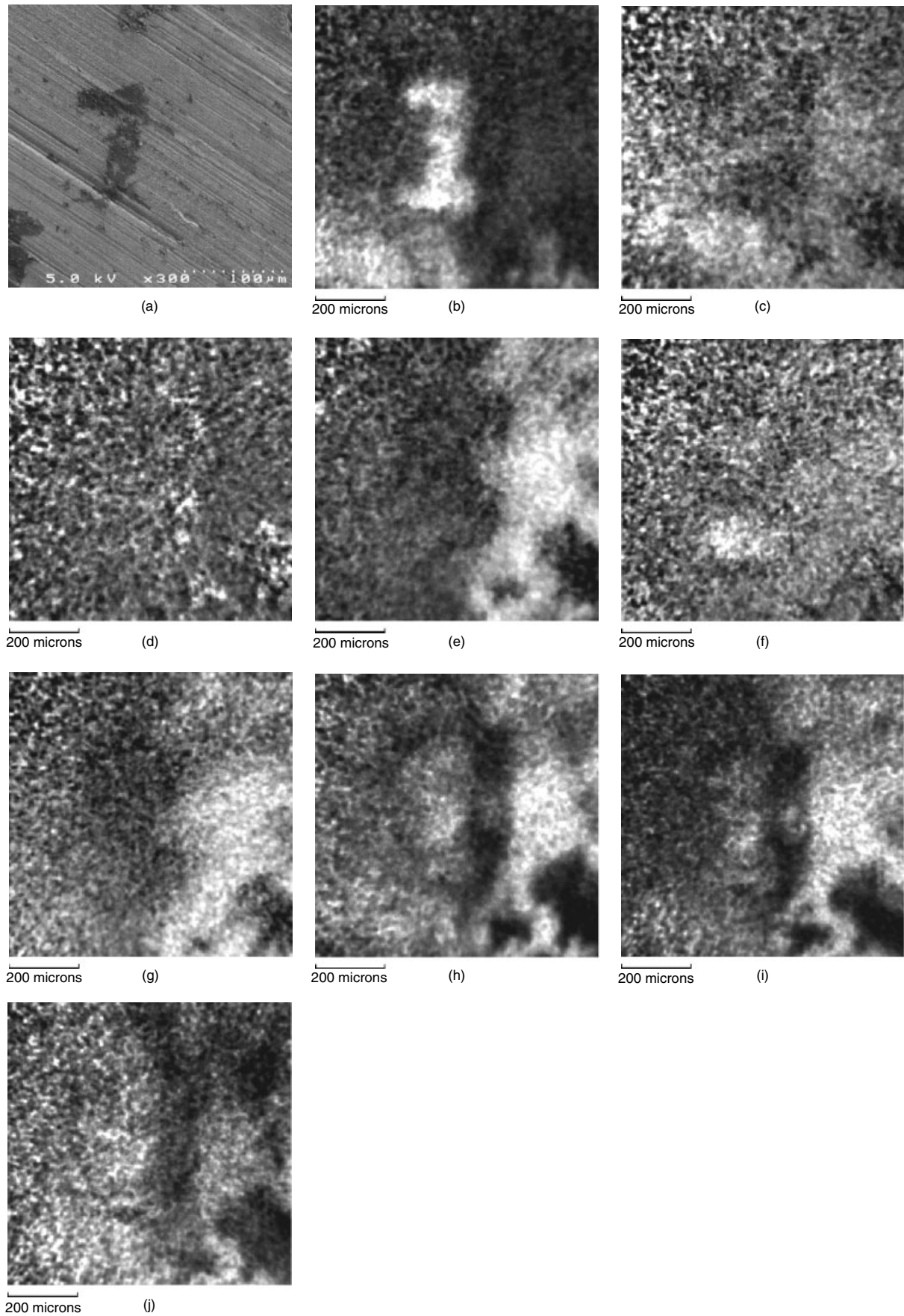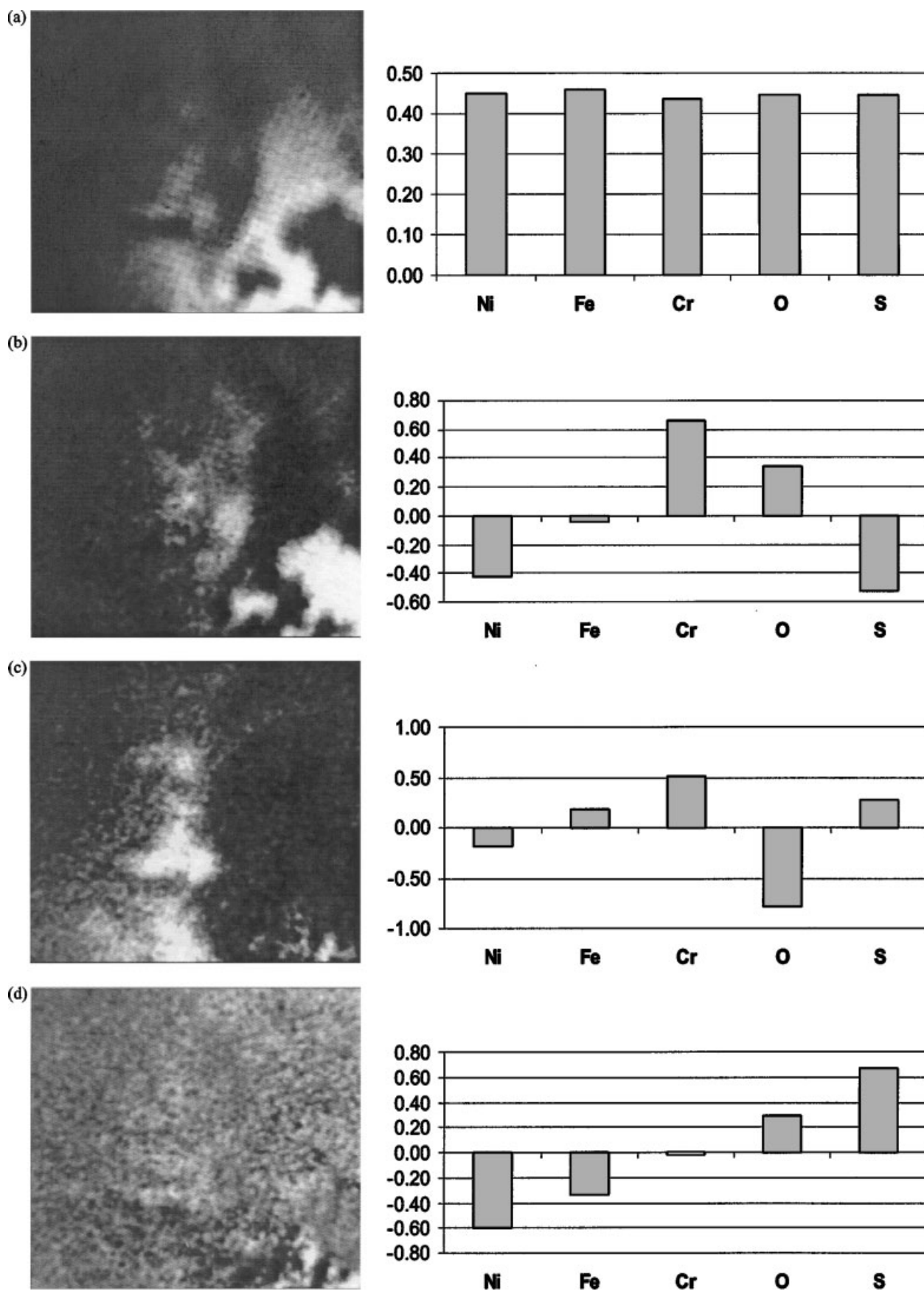
and sulphur (dark areas) are generally concentrated to the right of the defect. It is unclear how the nickel and sulphur are associated. The factor loads for PC 3 (variance of 1.5%) show that chromium, iron and sulphur are anti-correlated with oxygen and to a smaller degree nickel. The image score shows that chromium, sulphur and iron are concentrated in the defect area. Oxygen and nickel (dark areas) are located to the right of the defect and match the background-corrected images (Fig. 12). Finally, the factor loads for PC 4 (variance of 0.6%) show sulphur and oxygen anti-correlated with nickel and iron. The image score show that the sulphur and oxygen are distributed across the image. These results would indicate that sulphur is present in several different forms.

DISCUSSION

X-ray photoelectron spectroscopy imaging has allowed the electrochemical micro-electrode activity to be identified clearly and consistently in this series of corrosion experiments. Iron, chromium and nickel alloy components undergo anodic oxidation. All oxides are dissolved to some extent, because considerable erosion of the alloy is seen; however, chromium oxide is less soluble than the nickel and iron oxides at lower pH values, such as those present within a corrosion pit. Therefore the surface found inside the pit is dominated by chromium oxide. This does not, however, mean that any chromium oxide-rich area represents an anodic area; areas covered by a very thin chromium oxide film have undoubtedly become electrochemically passive and may even turn cathodic, as evidenced by the back-precipitation of microdeposits of iron and nickel oxides into the centre of some pits. In the case of sample A, the edges of the pit display evidence of more recent anodic activity: a thicker oxide highly enriched in chromium and depleted in nickel, with portions of the pit centre appearing to be passivated by a much thinner chromium film.

In all of the samples studied, sulphur species are identified at or near sites where pitting activity appears to have been most active recently. The sulphur most likely originates from impurities in the added salts; in cases where sulphur was deliberately added, it was in a sulphate form. However, for sample A, spectra taken in areas either near to an obvious site of anodic pitting or several hundreds of microns distant from that site consistently showed the presence of several sulphur chemical species, with sulphate, sulphite and sulphide being most prominent among them. We deduce therefore that sulphates deposited from solution undergo reduction to sulphide species; the presence of these may assist the initiation of pitting in areas already predisposed to failure, but there is no proof of sulphur as a primary causative agent.

Surface regions with elevated concentrations of iron represent areas of cathodic deposition of ferrous ions. For the E1 samples studied, these regions appear to be defined better and form a locus that is closer to the corresponding anodic region than was found for the E3 samples. Nickel cathodic deposition occurs in regions that are distinctly different than for iron. Deposition will occur only if the local cathodic potential exceeds the half-cell potential for the

particular reaction. Such regions are, generally further from the corresponding anode than was the case for iron.

The XPS imaging process has shown itself to be capable of producing a more well-defined assessment of the local electrochemical behaviour of iron and nickel species on this alloy surface. The background division method tested here appears to be quite effective in suppressing many of the effects of surface irregularity and its use is recommended for any metal corrosion study using XPS imaging, with the result that the corrected photoelectron intensities are much decreased by the process. Principal component analysis was useful for removing the effects of topography due to the roughness and slight curvature of the tube samples, the photoelectron background and artifacts from the CCD detector. The first principal component contained 85–95% of the variance in the data, which is attributed to topographic and background effects. The second principal component was found to contain the most useful and easily interpreted information about the elemental species. Samples A, B and C consistently showed that chromium was concentrated within the corrosion pit and nickel was deposited around the pit. These results were consistent with the corresponding background subtracted images. However, the PCA results for sample D did not match the corresponding background-subtracted images. The background-subtracted images show that the defect area is chromium-rich, whereas the PCA results indicate that chromium is mostly located outside the defect area. This could be due to the fact that sample D consists more of a thin surface oxide than a series of small pits. In general, the third and fourth principal components were found to represent only a very small portion of the variation in the data. In most cases, a correlation between sulphur and the other elements was observed, which was not readily obvious in the background-corrected images. The third PC from sample A shows a more oxidized sulphur species located away from the pit, whereas PC 4 shows a more reduced form of sulphur within the pit. The PCA results for samples B and C suggest a reduced sulphur species present within the pit region and on the surrounding surface of the tube. The results from sample D were more difficult to interpret, but it would appear that several sulphur species are present. Localized variations in the surface potential and pH will change the chemical state of sulphur.[16]

Despite low intensities, particularly at lower pass energies, chemical imaging of the local corrosion processes has been reasonably successful; regions containing higher concentrations of hydroxide and hydrates can be identified, even though the information defies interpretation with our present understanding of the local electrochemical processes. The ability to sense local oxide film thickness seems to have been very useful in the identification of regions passivated with a thin chromium oxide film. Corresponding images obtained using Auger imaging have provend to be more difficult to interpret, partly because surface contamination seems to have more influence in suppressing intensities from underlying species. This effect is one that cannot be ascribed entirely to the kinetic energies of the

carbon and oxide species involved and is therefore not completely understood.

CONCLUSIONS

(1) It is necessary to correct the XPS elemental and chemical maps for artifacts created by the inelastic background and by topographic effects produced from the roughness and curvature of the corroded tube samples. A background subtraction $(S - B)$ was first applied to remove the inelastic background, followed by a background division $((S - B)/B)$ to remove topographic effects.

(2) Principal component analysis proved useful as an alternative method to remove image artifacts produced by the CCD detector and sample topography. Correlation was observed between the major elements (nickel, iron, chromium, oxygen and sulphur), which aided in the identification of anodic sites.

(3) Auger images were collected, background-corrected and then compared with XPS images of the same corrosion pit. Owing to the higher surface sensitivity of Auger compared with XPS, it was necessary to sputter the sample for 5 s to remove the carbon overlayer. The resulting Auger maps have higher spatial resolution compared with the XPS images and also show similar anodic sites that are rich in chromium. Although the Auger maps are very detailed, the chemical information of the species present cannot be determined by this technique.

(4) The XPS image analyses identified chromium-rich anodic sites and cathodic back-deposition of nickel and iron. Sulphur, originally present as a sulphate impurity, was found in active pits and is believed to have been reduced to various sulphide species.

REFERENCES

1. Francis JT, McIntyre NS, Davidson RD, Ramamurthy S, Brennenstühl AM, McBride A, Roberts A. *Surf. Interface Anal.* 2002; **33**: 29.
2. Brennenstühl AM, McBride A, Francis JT, Ramamurthy S, Bret BE, Pagan SM. COG-99-127, CANDU Owners Group-Final report, 1999.
3. Gonzalez FS, Spekkens P. *Nucl. J. Can.* 1987; **1**: 129.
4. Mardia K, Kent JT, Bibby JM. *Multivariate Analysis.* Academic Press: London, 1979; 213.
5. Kargacin ME, Kowalski BR. *Anal. Chem.* 1986; **58**: 2300.
6. Massart DL, Vandeginste BGM, Buydens LMC, De Jong S, Lewi PJ, Smeyers-Verbeke J. *Handbook of Chemometrics and Qualimetrics.* Elsevier: Amsterdam, 1997; 519.
7. Biesinger MC, Paepegaey PY, McIntyre NS, Harbottle RR, Petersen NO. *Anal. Chem.* 2002; **74**: 5711.
8. Artyushkova K, Fulghum JE. *Surf. Interface Anal.* 2004; **36**: 1304.
9. Artyushkova K, Fulghum JE. *Surf. Interface Anal.* 2002; **33**: 185.
10. Allen GC, Hallam KR, Eastman JR, Graveling GJ, Ragnarsdottir VK, Skuse DR. *Surf. Interface Anal.* 1998; **26**: 518.
11. Piantadosi C, Janieniak M, Skinner W, Smart RS-C. *Miner. Eng.* 2000; **13**: 1377.
12. Crone M, Barshire IR, Prutton M, Kenny PG. *Surf. Interface Anal.* 1994; **22**: 581.
13. Hoppe HW, Strehblow HH. *Surf. Interface Anal.* 1989; **14**: 121.
14. McIntyre NS, Rummery TE, Cook MG, Owen D. *J. Electrochem. Soc.* 1976; **123**: 1164.
15. Biesinger MC, Brown C, Mycroft JR, Davidson RD, McIntyre NS. *Surf. Interface Anal.* 2004; **36**: 1550.
16. Harper SL, Miglin BP, Monter JV, Theus GJ. *Proc. Third International Symposium on Environmental Degradation of Materials in Nuclear Power Systems—Water Reactors*, Traverse City, Michigan, 1987; 457.